Exceedingly small moment itinerant ferromagnetism of single crystalline $La_5Co_2Ge_3$

S. M. Saunders,[1,2] L. Xiang,[1,2] R. Khasanov,[3] T. Kong,[1,2,*] Q. Lin,[1,4] S. L. Bud'ko,[1,2] and P. C. Canfield[1,2]

[1]*Ames Laboratory, U.S. DOE, Iowa State University, Ames, Iowa 50011, USA*

[2]*Department of Physics and Astronomy, Iowa State University, Ames, Iowa 50011, USA*

[3]*Laboratory for Muon Spin Spectroscopy, Paul Scherrer Institute, 5232 Villigen, Switzerland*

[4]*Department of Chemistry, Iowa State University, Ames, Iowa 50011, USA*

(Received 25 February 2020; accepted 13 May 2020; published 1 June 2020)

Single crystals of monoclinic $La_5Co_2Ge_3$ were grown using a self-flux method and were characterized by room-temperature powder x-ray diffraction, anisotropic temperature- and field-dependent magnetization, temperature-dependent resistivity, specific heat, and muon spin rotation. $La_5Co_2Ge_3$ has a Curie temperature (T_C) of 3.8 K and clear signatures of ferromagnetism in magnetization and μSR data, as well as a clear loss of spin disorder scattering in resistivity data and a sharp specific heat anomaly. The magnetism associated with $La_5Co_2Ge_3$ is itinerant has a change in the entropy at T_C of $\simeq 0.05R \ln 2$ per mol Co and has a low-field saturated moment of $\sim 0.1\ \mu_B$/Co, making it a rare, itinerant, small moment, low-T_C compound.

DOI: 10.1103/PhysRevB.101.214405

Magnetism in metallic compounds has typically been described in a local moment or itinerant moment picture. The local moment description has been studied across many systems, due, in part, to the convenience of rare-earth elements containing partially filled $4f$ shells which provide well defined, local magnetic moments [1]. There are fewer examples of itinerant magnetism, especially ferromagnetic systems with very low Curie temperature T_C and saturated magnetic moment μ_{sat}. For example, Sc_3In [2], $ZrZn_2$ [3], MnSi [4], $LuFe_2Ge_2$ [5,6], and TiAu [7] have been suggested to be itinerant with low transition temperatures: $T_C = 6$ and 35 K for the ferromagnetic Sc_3In and $ZrZn_2$, respectively, and $T_N = 29$, 9, and 36 K for the antiferromagnetic MnSi, $LuFe_2Ge_2$, and TiAu, respectively.

In this manuscript, we report the discovery and basic properties of the itinerant ferromagnet (IFM) $La_5Co_2Ge_3$. $La_5Co_2Ge_3$ is composed of 50% non-moment-bearing La, 30% Ge, and only 20% Co; transport and thermodynamic measurements exhibit a Curie temperature of $T_C = (3.8 \pm 0.1)\,K$, which is one of the lowest reported transition temperatures for an ordered, stoichiometric IFM. Temperature- and field-dependent magnetization measurements reveal $\mu_{eff} = (1.10 \pm 0.05)\,\mu_B$/Co, whereas the low-field $\mu_{sat} = 0.1\,\mu_B$/Co leading to a Rhodes-Wohlfarth ratio [8] of 4.9. In addition, specific heat data show a greatly reduced loss of entropy, $0.05R \ln 2$ per mol Co, associated with the transition. Muon spin rotation (μSR) measurements indicate static moments and internal fields consistent with a greatly reduced ordered moment magnitude when compared to full-moment Co.

Single crystals of $La_5Co_2Ge_3$ were grown using a self-flux solution growth method [9–11]. The initial composition of the three elements was La:Co:Ge = 45:45:10. The starting elements (Co (99.9%), Ge (Alfa Aesar 99.9 + %), and La (Ames Lab 99.9%)) were combined in a three-cap tantalum crucible [9,10] and sealed in a fused silica ampoule under a partial argon atmosphere. The ampoule was then heated to 1180 °C, held at 1180 °C for 4 hours and slowly cooled to 800 °C over 40 hours at which point the remaining solution was decanted with the assistance of a centrifuge. The crystals of $La_5Co_2Ge_3$ grew in thin plates as well as long blades, as shown in Fig. 1. The crystals are not air sensitive.

$La_5Co_2Ge_3$ is isostructural to $Pr_5Co_2Ge_3$ [11]; the crystal structure was established at room temperature and ambient pressure using a Rigaku Miniflex powder x-ray diffractometer (Cu K_α radiation). Samples were prepared by grinding a single crystal into powder, which was then mounted and measured on a single crystal Si, zero-background sample holder. A typical x-ray diffraction pattern, where all major peaks are consistent with the $La_5Co_2Ge_3$ monoclinic structure, is shown in Fig. 1 and discussed in further detail in the Appendix. When growing $La_5Co_2Ge_3$, two morphologies emerged in the growth crucible, with representative examples shown in Fig. 1. However, when studied by powder x-ray diffraction, the powder x-ray patterns for platelike and bladelike crystals are identical. As determined by back reflection Laue diffraction, the direction perpendicular to the face of the crystal is the a^* direction, which is perpendicular to b and c.

Back reflection Laue images were collected at room temperature. The incident x rays were produced by a 40 kV and 15 mA power source through a 0.5 mm diameter circular aperture and collected over 300 s. Crystal systems with a monoclinic unit cell (Fig. 9 in the Appendix), like $La_5Co_2Ge_3$, are part of the $2/m$ Laue class. As such, they will exhibit twofold symmetry in the back reflection pattern, which is shown in the inset to Fig. 1. Using this image and the corresponding unit cell data (Table I in the Appendix), the peaks were indexed with the assistance of CLIP (the Cologne Laue indexation program) [12] and the specific orientation of the crystal that would give rise to the resultant peaks was identified.

*Present Address: Department of Physics, University of Arizona, Tucson, AZ 85721, USA; tkong@email.arizona.edu

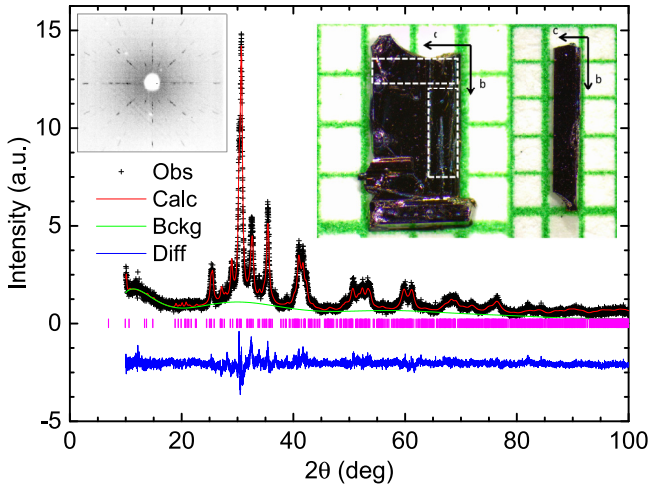

FIG. 1. Powder x-ray diffraction data for $La_5Co_2Ge_3$. Vertical pink lines represent expected peak positions for structural data (Tables I and II in the Appendix). Inset: (left) back reflection Laue diffraction pattern with beam perpendicular to the face of the plate, showing the twofold mirror symmetry expected for a monoclinic system. (Right) Representative crystal morphologies of $La_5Co_2Ge_3$ shown on mm grid. A typical plate (left) and blade(right) are shown. Dashed lines outline samples which were cut and measured for resistivity (see text).

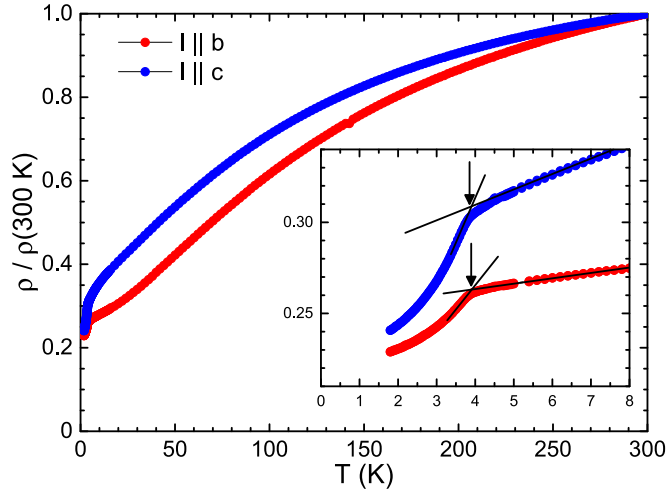

FIG. 2. Zero-field, normalized, in-plane resistivity vs temperature for current flowing along b or c axis [(inset) low-temperature zoom of resistivity vs temperature with the criterion for determining T_C indicated by the lines and arrows]. At $T = 300$ K, $\rho_b = 220\ \mu\Omega$ cm, and $\rho_c = 390\ \mu\Omega$ cm.

DC magnetization measurements were performed in a Quantum Design Magnetic Property Measurement System 3 (MPMS 3), superconducting quantum interference device (SQUID) magnetometer ($T = 1.8$–300 K, $H_{max} = 70$ kOe). All samples were manually aligned to measure the magnetization along the desired axis. A bladelike crystal was selected with measurements performed perpendicular to the face of the blade and parallel to the face of the blade. Measurements conducted perpendicular to the blade are perpendicular to the b-c plane (i.e., parallel to a^*). Samples which were aligned parallel to the plate are in either the b or c direction (see Fig. 1). For measurements with $H||b$ or c, the sample was mounted on a quartz rod and attached by GE varnish.

Resistivity measurements were performed using a standard four-probe technique with the temperature environment provided by a MPMS with $I = 1$ mA supplied by an LR-700 resistance bridge. As shown in Fig. 1, platelike samples allowed for the creation of samples that had current along the b or the c axis. Epotek-H20E epoxy was used to connect Pt wires to the sample so that the current was flowing in the desired direction.

Specific heat measurements between $T = 1.8$ and 50 K were performed in a Quantum Design Physical Property Measurement System (PPMS) utilizing the relaxation technique with fitting of the whole temperature response of the microcalorimeter. A platelike sample was mounted on the microcalorimeter platform using a small amount of the Apiezon N grease. A 2% temperature rise at each measurement point was used. The addenda (contribution from the grease and sample platform) was measured separately and subtracted from the data using PPMS software.

The Zero-field muon spin rotation (μSR) measurements were performed at the πE1 beamline by using Dolly spectrometer (Paul Scherrer Institute, PSI Villigen, Switzerland). The ^{4}He cryostat equipped with the ^{3}He inset (base temperature $\simeq$0.26 K) was used. Samples were mounted on a thin copper foil ($\simeq$10 μm), which was transparent for positive surface muons used in our studies.

Resistivity measurements (Fig. 2) show hat the samples are metallic; at $T = 300$ K, $\rho_b = 220\ \mu\Omega$ cm, and $\rho_c = 390\ \mu\Omega$ cm. The crystals that were measured have residual resistance ratios [RRR $= \rho(300\text{ K})/\rho(2\text{ K})$] ranging from 3–5. Below $T = 4$ K there is a sharp drop in resistivity with an onset temperature, $T_C = 3.8$ K, indicated by the arrows in the inset of Fig. 2.

The temperature-dependent magnetic susceptibility, $\chi \equiv M/H$, for $La_5Co_2Ge_3$ is shown in Fig. 3. The low temperature, $H = 50$ Oe, M/H data (Fig. 3, inset) show a clear transition below 4.0 K. At the higher temperature, $H = 1$ kOe, magnetic susceptibility data manifest a clear Curie-Weiss-like behavior that can be described by

$$\frac{M}{H} = \frac{C}{T - \Theta} + \chi_0, \tag{1}$$

where C is the Curie Constant defined as $C = N(\mu_{\text{eff}}\mu_B)^2/3k_B$, Θ is the Weiss temperature arising from interactions between spins, χ_0 is a T-independent contribution. When fitting the temperature-dependent M/H data for 20 K $\leqslant T \leqslant$ 100 K, values of $\mu_{\text{eff}} = 1.2\,\mu_B$/Co, $\Theta = 0.5$ K, $\chi_0 = 0.007$ emu mol^{-1} Co^{-1}, $\mu_{\text{eff}} = 1.0\,\mu_B/Co$, $\Theta = -13$ K, $\chi_0 = 0.008$ emu mol^{-1} Co^{-1}, and $\mu_{\text{eff}} = 1.1\,\mu_B/Co$, $\Theta = 1.3$ K, $\chi_0 = 0.007$ emu mol^{-1} Co^{-1} were found for H parallel to the a^*, b, and c directions, respectively. Uncertainties for μ_{eff} and Θ are determined to be $\pm 0.1\,\mu_B$/Co and ± 4 K respectively, due primarily to the uncertainties in the measurement of the mass. For all directions, Curie-Weiss fits result in a high-temperature

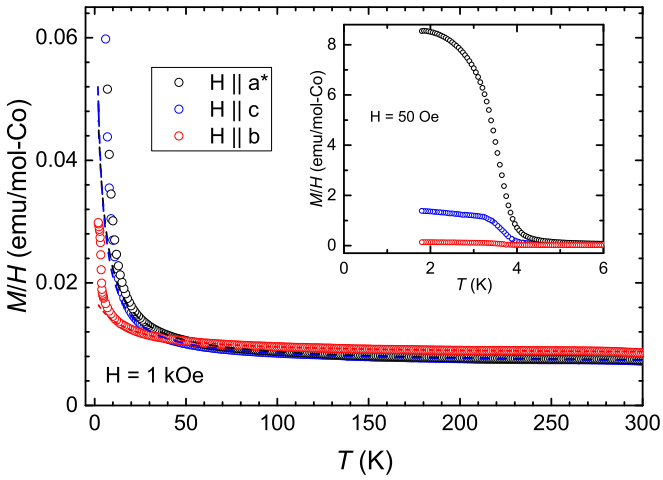

FIG. 3. Anisotropic magnetic susceptibility of $La_5Co_2Ge_3$ measured at $H = 1$ kOe. Dashed lines are the Curie-Weiss fits as described in the main text. (Inset) Low-temperature zoom of anisotropic magnetic susceptibility at $H = 50$ Oe.

paramagnetic effective moment $\mu_{\rm eff} \sim 1.1\mu_B/Co$. The positive (negative) sign of Weiss temperature Θ indicates dominating ferromagnetic (antiferromagnetic) interactions. In addition, a crossing of M/H curves measured with field applied along different directions is observed at ~40 K. This is due to the combination that χ_0 for $H||b$ is larger than those for $H||a^*$, c, and that the two curves (with $H||a^*$, c) with very small positive Θ values rising faster than the curve (with $H||b$) with a larger, negative Θ value. $M(T)$ data collected on a significantly larger, polycrystalline sample, measured in a 64 kOe applied field (see Fig. 10 in the Appendix), gave values of $\mu_{\rm eff} = (1.10 \pm 0.05)\,\mu_B/Co$ and $\Theta = (-10.7 \pm 0.2)$ K from a fit for 10 K $\leqslant T \leqslant$ 300 K.

Anisotropic magnetization versus field data (Fig. 4) were taken for $|H| \leqslant 70$ kOe at $T = 2$ K. A striking anisotropy is readily apparent. Whereas for $H||a^*$ and $H||c$ there is a

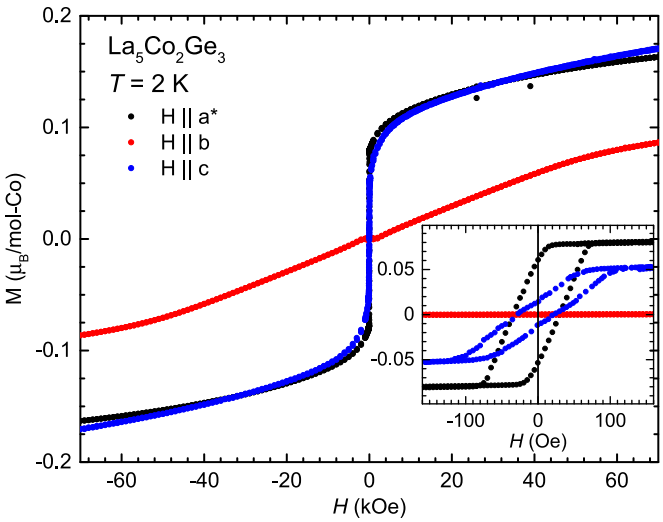

FIG. 4. Anisotropic magnetization vs field isotherms of $La_5Co_2Ge_3$. (Inset) Low-field zoom of data revealing hysteresis for $H \,||\, a^*$ and $H \,||\, c$.

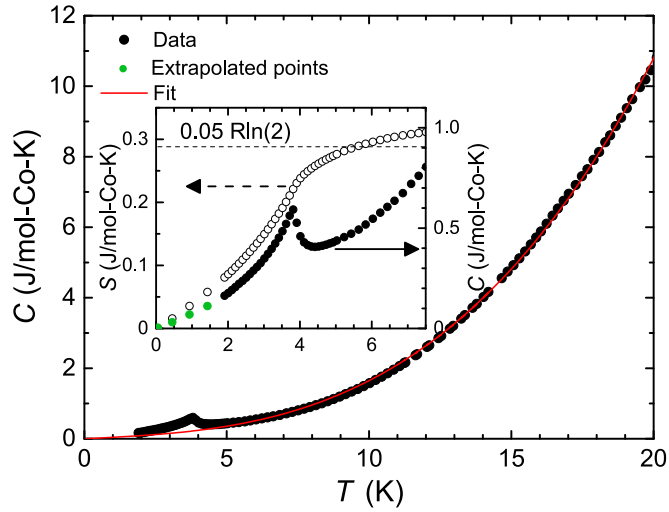

FIG. 5. Specific heat vs temperature [(inset) low-temperature zoom of entropy vs temperature (left axis) and heat capacity vs temperature (right axis); data were extrapolated to 0, 0 (green points) to allow for evaluation of entropy). Red line shows Debye fit to data (see text).

low-field saturation to an ≃0.1 μ_B per mol Co value, for $H||b$, the $M(H)$ data have no such feature. For fields well above their initial saturations, the $H||a^*$ and $H||c$ $M(H)$ data show a very similar, gradual increase with H as does the $H||b$ data. The inset to Fig. 4 shows that for the two easier axes there is clear hysteresis that can be associated with domain pinning. Utilizing a linear fit of the data just above saturation to extrapolate to $H = 0$, we obtain $\mu_{\rm sat} = 0.08\,\mu_B$ per mol Co, $\mu_{\rm sat} = 0\,\mu_B$ per mol Co, and $\mu_{\rm sat} = 0.05\,\mu_B$ per mol Co for the a^*, b, and c directions, respectively.

Taken as a whole, the $M(T, H)$ data shown in Figs. 3 and 4 suggest that below T_C, $La_5Co_2Ge_3$ becomes a small moment, easy-plane ferromagnet that has a more isotropic, nonlinear, but smoothly varying $M(H)$ behavior superimposed on top of the low-field saturation.

Specific heat data, as shown in Fig. 5, exhibit a cusp with a maxima at $T = 3.8$ K. Given that our resistivity data show a similar transition at 3.8 K and our low-field $M(T)$ data show a sharp rise around 3.9 K, we conclude that $La_5Co_2Ge_3$ becomes ferromagnetic below $T_C = (3.8 \pm 0.1)$ K. Specific heat data were fit using $C = \gamma T + \beta T^3$ over the region 10 K $< T <$ 15 K which is linear in C/T versus T^2. Through this fit, we obtain coefficients of $\gamma \approx 40$ mJ mol^{-1} K^{-2} and $\beta \approx 2.7$ mJ mol^{-1} K^{-4}. We then used these fitted values of γ and β to extrapolate data points to $T = 0$ K and to estimate the electron and phonon contributions to the specific heat (shown as a red line in the figure). To estimate the entropy associated with the magnetic transition, we subtracted the inferred electron and phonon contributions from the specific heat data and integrated with respect to T. The entropy inferred from the specific heat data (inset of Fig. 5) reveals the total magnetic entropy of the transition is roughly $0.05R\ln(2)$ per Co.

Taken together, the data so far strongly suggest that $La_5Co_2Ge_3$ is a small moment ferromagnet; in order to test this microscopically, we performed μSR measurements on a

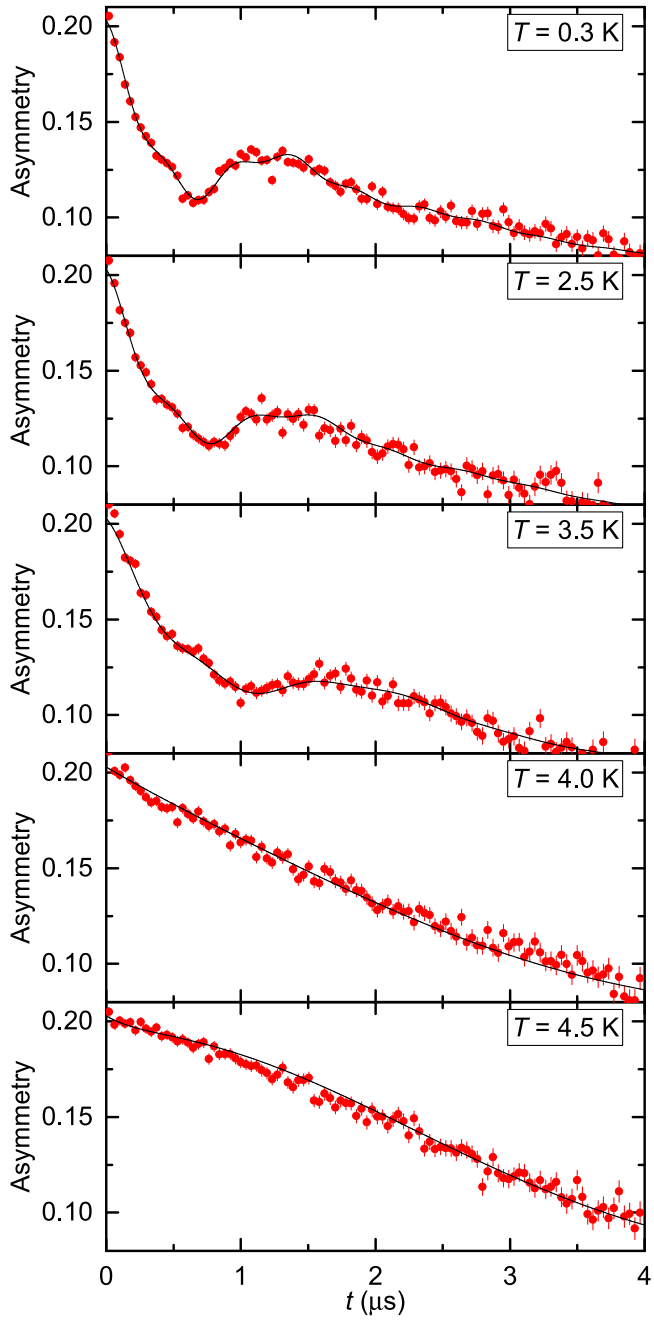

FIG. 6. Zero-field μSR spectra data of $La_5Co_2Ge_3$. Solid lines are fits made with two cosine signals with zero initial phase.

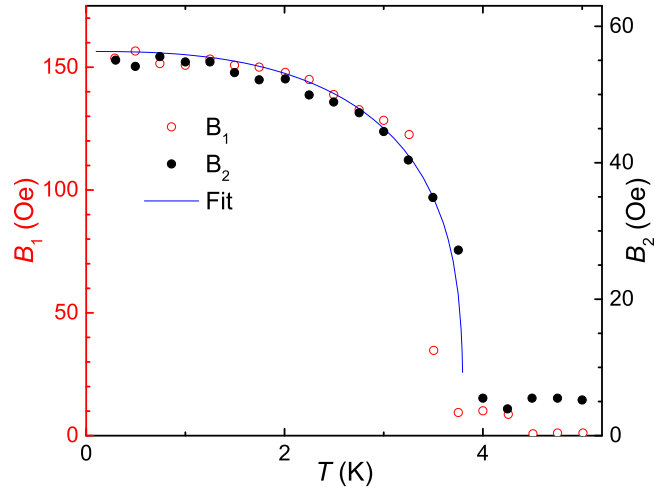

FIG. 7. Internal field vs temperature of $La_5Co_2Ge_3$. The fit was made by assuming two independent oscillatory components. The internal fields (B_1 and B_2) and the transversal relaxations (Λ_1 and Λ_2) were assumed to be different. The longitudinal relaxations Λ_L were assumed to be the same. The relative volume fraction corresponding to the higher field is ~20% and the one corresponding to the lower field is ~80%.

sample in the 0.26 K $\leqslant T \leqslant$ 5 K temperature range (Figs. 6, 7, and 12). (See Appendix for details of μSR measurements and analysis). For $T < 4$ K, we found static magnetic order. The magnetic order is found to be commensurate, as the fit in Fig. 6 was made with two cosine signals with zero initial phase. The presence of two internal fields suggests the presence of two sites within the crystal lattice where the muons come into ~20% of muons stop in a higher field site and ~80% stop in a lower field site (Fig. 7).

Although $La_5Co_2Ge_3$ does order magnetically, we do not observe internal fields consistent with full Co moments (see Fig. 7). The larger internal field $B_{\mathrm{int},1}$ only reaches 150 Oe, which is approximately one order of magnitude smaller than expected for full Co moments [13]. Such low field for the full Co moment might be expected only for highly symmetric muon stopping site, which is normally not a case for real systems. Thus, the obtained internal fields results are consistent with our small saturated moment (Fig. 4) and $\Delta S \simeq 0.05R\ln(2)$ per Co (Fig. 5). Both of the internal fields exhibit similar temperature dependencies; when fitting the data in Fig. 7 to the power law $B = B_0(1-(T/T_C)^{\alpha})^{\beta}$, we find that $\beta = 0.293$ which is consistent with three-dimensional magnetic order ($\beta_{3D} = 1/3$).

The difference between the effective moment inferred from magnetization versus temperature data (Fig. 3) and the low-field saturated moment from magnetization versus field data (Fig. 4) can be understood by considering the Rhodes-Wohlfarth ratio q_c/q_s [2,8,14], where

$$\begin{aligned} \mu_{\mathrm{eff}}^2 &= q_c(q_c+2)\mu_B^2, \\ \mu_{\mathrm{sat}} &= q_s\mu_B, \\ q_c/q_s &= (-1+\sqrt{1+(\mu_{\mathrm{eff}}/\mu_B)^2})/(\mu_{\mathrm{sat}}/\mu_B). \end{aligned} \tag{2}$$

We can compare $La_5Co_2Ge_3$ to other itinerant magnetic systems as shown in Fig. 8. The Rhode-Wohlfarth ratio can be thought of as a measure of the change in magnetic moment as you change temperature (μ_{eff} inferred from the high-temperature data, μ_{sat} inferred from the low-temperature data). For $La_5Co_2Ge_3$, $q_c/q_s = 4.9$. Figure 8 shows $La_5Co_2Ge_3$ is an intriguing combination of an ordered, line compound and one of the lowest Curie temperatures for transition-metal based ferromagnetism.

The thermodynamic, transport, and microscopic data presented on $La_5Co_2Ge_3$ all suggest that below 3.8 K there is small moment, itinerant, ferromagnetic ordering. The low-temperature, linear specific heat coefficient, γ, is also consistent with this. $\gamma = 40$ mJ mol^{-1} K^{-2} is a

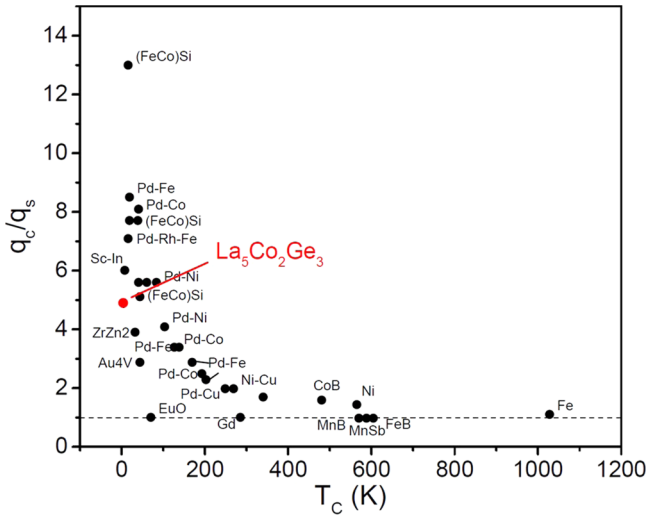

FIG. 8. Rhodes-Wohlfarth ratio q_c/q_s vs Curie temperature T_C for various materials [3,14]. $La_5Co_2Ge_3$ is shown in red, where q_c was determined from the effective moment obtained by fitting data from Fig. 3 and q_s determined from the saturated moment obtained from Fig. 4.

rather large value, even for a compound with ten atoms per formula unit. This value can be put into context well by comparing it to γ values for the $Y(Fe_xCo_{1-x})_2Zn_{20}$ series [15]. Although YFe_2Zn_{20} does not order magnetically, it is exceptionally close to the Stoner limit and has a $\gamma = 50$ mJ mol^{-1} K^{-2}. YCo_2Zn_{20}, on the other hand, is far from this limit and has a $\gamma = 20$ mJ mol^{-1} K^{-2} (yielding a fairly standard 1 mJ mol^{-1} atomic^{-1} K^{-2} value). Using a similar 1 mJ mol^{-1} atomic^{-1} K^{-2} value for generic broad-band background, $La_5Co_2Ge_3$ has roughly 15 mJ mol^{-1} Co^{-1} K^{-2}, similar to the value found for Fe in YFe_2Zn_{20}. Comparison can also be made to $LuFe_2Ge_2$ [5,6] which has a spin-density wave type of itinerant antiferromagnetic ordering near 9 K and a γ value of roughly 65 mJ mol^{-1} K^{-2}.

Taken together, our data indicate that $La_5Co_2Ge_3$ is an ordered compound at the limit of low T_C and high q_c/q_s. As such, it offers a chance to study how much further T_C can be pushed, or tuned toward $T = 0$, either by pressure or substitution before the anticipated avoided quantum criticality that is associated with metallic ferromagnetic systems is encountered [16–19].

We would like to thank A. Kreyssig for useful discussions and R. A. Ribeiro for assistance with magnetization measurements. This work is supported by the US DOE, Basic Energy Sciences under Contract No. DE-AC02-07CH11358 and the Gordon and Betty Moore Foundation's EPiQS Initiative through Grant No. GBMF4411.

APPENDIX A: STRUCTURE REFINEMENT

Single crystal x-ray diffraction intensity data for $La_5Co_2Ge_3$ were collected at room temperature using a Bruker SMART APEX II diffractometer (Mo K_α radiation, $\lambda = 0.71073$ Å). Data reduction, integration, unit cell refinements, and absorption corrections were done with the aid of subprograms in APEX2 [20,21]. Space group determination, Fourier synthesis, and full-matrix least-squares refinements on F2 were carried out by in SHELXTL 6.1 [22]. The direct methods in space group C2/m yielded a structural model containing five La, two Co, and three Ge independent sites. Separate refinements on occupancy parameters for Co and Ge sites revealed no partial occupancy and no Co/Ge mixing in this structure. Table I gives the crystal data and structure refinement for $La_5Co_2Ge_3$ and Table II lists the refined atomic positions and equivalent isotropic displacement parameters.

TABLE I. Crystal data and structure refinement for $La_5Co_2Ge_3$.

Empirical formula	$La_5Co_2Ge_3$
Formula weight	1030.2 g/mol
Space group, Z	C2/m, 4
Unit cell dimensions	$a = 18.354(4)$ Å
	$b = 4.3479(9)$ Å
	$c = 13.279(3)$ Å
	$\beta = 109.592(2)^\circ$
Z	4
Density (calculated)	6.663 g/cm^3
Reflections collected	30592 [$R_{int} = 0.0384$]
Data / restraints / parameters	5893 / 0 / 62
Goodness-of-fit on F^2	1.179
Final R indices [I $> 2\sigma$(I)]	$R1 = 0.0342$, $wR2 = 0.0530$
R indices (all data)	$R1 = 0.0512$, $wR2 = 0.0564$
Largest diff. peak and hole	1.316 and -1.486 e Å^{-3}

The structure of $La_5Co_2Ge_3$ is part of a $R_5Co_2Ge_3$ family and represents a new structural type, with Pearson symbol of mS40. This structure type has been previously reported by Lin *et al.* [11]. The y coordinates for all atoms in this structure equal to zero, meaning that atoms in this structure are located either on planes at $y = 0$ or $y = 1/2$ arising from the C center in space group C2/m. The structure appears as the ethylenelike Co_2Ge_4 fragments and the polyacenelike ribbons immersed in a sea of the rare-earth ions, cf. Fig. 9. In this structure, Co-Co and Co-Ge bonds show the strongest covalent bonding interactions, as indicated by respective bond distances (dCo − Co = 2.325–2.358 Å,

TABLE II. The refined atomic positions and equivalent isotropic displacement parameters for $La_5Co_2Ge_3$.

Atom	Wyck.	Symm.	x	y	z	U_{eq} (Å^2)
La1	4i	m	0.0013(1)	0	0.1371(1)	0.0015(1)
La2	4i	m	0.3171(1)	0	0.4397(1)	0.0015(1)
La3	4i	m	0.3228(1)	0	0.1090(1)	0.0014(1)
La4	4i	m	0.4998(1)	0	0.3616(1)	0.0015(1)
La5	4i	m	0.6819(1)	0	0.2300(1)	0.0014(1)
Co1	4i	m	0.0670(1)	0	0.5212(1)	0.0017(1)
Co2	4i	m	0.5661(1)	0	0.0240(1)	0.0019(1)
Ge1	4i	m	0.1325(1)	0	0.7121(1)	0.0015(1)
Ge2	4i	m	0.1323(1)	0	0.3749(1)	0.0015(1)
Ge3	4i	m	0.1466(1)	0	0.0493(1)	0.0015(1)

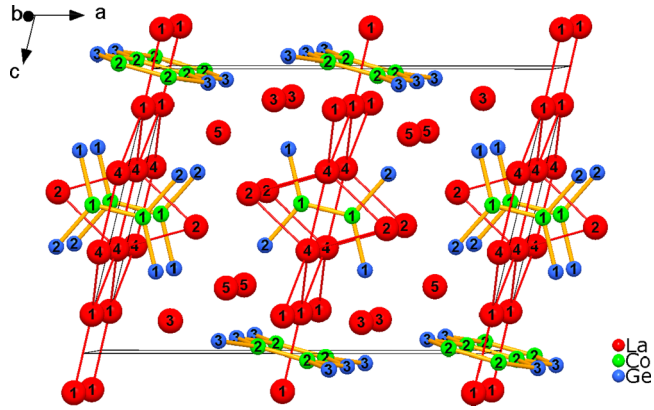

FIG. 9. Crystal structure of $La_5Co_2Ge_3$.

dCo − Ge = 2.494–2.558 Å). Notably, the separations for La1-La4, La2-La4, and La4-La4 pairs are smaller than the sum of Pauling's metallic radii (3.648 Å) [23], suggesting considerable covalent interactions among them. These pairs form two-dimensional honeycomb nets parallel to the bc plane, hexagons in the net are perpendicularly penetrated by Co-Co bonds (Fig. 1). Sandwiched by the forgoing honeycomb nets, La2, La3, and La5 atoms form slabs of edge-sharing tetrahedra with slightly longer La-La distances (3.647–3.924 Å).

APPENDIX B: MAGNETIZATION MEASUREMENT AND ANALYSIS ON POWDER SAMPLE

In order to better measure the high-temperature Curie-Weiss behavior, a powder sample was made by grinding 95 mg of single crystals and was measured in a field of 64 kOe as a function of temperature. The temperature-dependent M/H data (Fig. 10) manifest a clear Curie-Weiss-like behavior for 10 K $\leqslant T \leqslant$ 300 K. When the data are fit to Eq. (1) with the Curie constant $C = N(\mu_{\text{eff}}\mu_B)^2/3k_B$, values of $\mu_{\text{eff}} = (1.10 \pm 0.05)\,\mu_B/Co$, $\Theta = (-10.7 \pm 0.2)\,K$, and $\chi_0 = 0.0038 \pm 0.0002$ emu mol^{-1} Co^{-1} were found. The

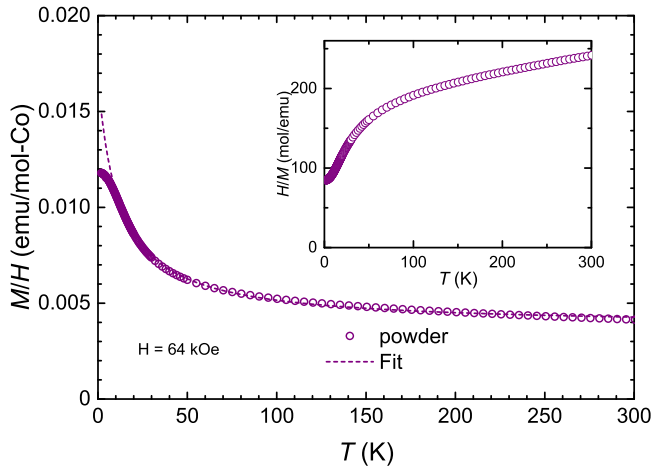

FIG. 10. Magnetic susceptibility of $La_5Co_2Ge_3$ powder measured at $H = 64$ kOe, with dashed line indicating fit of data. (Inset) Inverse magnetic susceptibility of $La_5Co_2Ge_3$ powder measured at $H = 64$ kOe.

H/M data (Fig. 10, inset) demonstrate that the χ_0 term is relatively large over the whole temperature range and does not allow for insightful use of such plots.

APPENDIX C: ITINERANT FERROMAGNETISM ANALYSIS BY SPIN-FLUCTUATION THEORY

The itinerant nature of the ferromagnetism can be further analyzed by using Takahashi's spin-fluctuation theory for weak (small ordered moment) itinerant ferromagnets [24,25]. In Takahashi's theory, to capture the spin fluctuation, the expansion of the free energy $F(M,T)$ for a ferromagnet is kept up to sixth order,

$$F(M,T) = F(0,T) + \tfrac{1}{2}a_2(T)M^2 + \tfrac{1}{4}a_4(T)M^4 + \tfrac{1}{6}a_6(T)M^6 - MH, \tag{C1}$$

where the prefactors $a_4(T)$ and $a_6(T)$ are related to the spin fluctuation. Minimizing free energy gives

$$H = a_2(T)M + a_4(T)M^3 + a_6(T)M^5. \tag{C2}$$

For the ground state ($T = 0$ K), one considers the expansion of $F(M,T)$ up to fourth order and obtains

$$H = \frac{F_1}{(g\mu_B)^4 N_0^3}\left(M^2 - M_0^2\right)M, \tag{C3a}$$

$$F_1 = \frac{2k_B T_A^2}{15cT_0}, \tag{C3b}$$

where $c = 1/2$ is a constant, N_0 is the number of magnetic atoms, M_0 is the ordered moment in the ground state, T_0 and T_A (in the temperature units K) are the ferromagnetic spin fluctuation parameters which measure the energy width and wave vector width of the spin fluctuation, respectively. Thus, in the ground state, the magnetic isotherm is influenced by the zero-point spin fluctuation F_1, which depends on the ferromagnetic spin fluctuation parameters T_0 and T_A. These two parameters can be inferred from magnetic isotherm data:

$$M^2 = \frac{1}{\left(248.2\frac{\text{Oe}}{\text{K}}\right)\left(\frac{T_A^2}{T_0}\right)}\frac{H}{M} + M_0^2, \tag{C4a}$$

$$M_0 \simeq 2\sqrt{C_{4/3}\frac{5T_0}{T_A}}\left(\frac{T_C}{T_A}\right)^{2/3}, \tag{C4b}$$

where $C_{4/3}$ is a constant ~1. Based on Eqs. C3(a) and 5(b), T_0 and T_A can be calculated from the slopes and intercepts of M^2 versus H/M plots (Arrott plot) at low temperatures (where M^2 versus H/M is linear at high fields) [26], given that T_C is known (or can be also determined from Arrott plots).

For the temperatures close to T_C, the magnetic isotherms are predominately influenced by temperature-induced spin fluctuation [a_6 term in Eq. (C2)] instead of zero-point spin fluctuation. At T_C, a_2 and a_4 are zero and Eq. (C2) can be expressed as

$$\frac{M^4}{H/M} = \frac{1}{\left(4.671\frac{\text{Oe}}{\text{K}}\right)\left(\frac{T_A^3}{T_C^2}\right)}. \tag{C5}$$

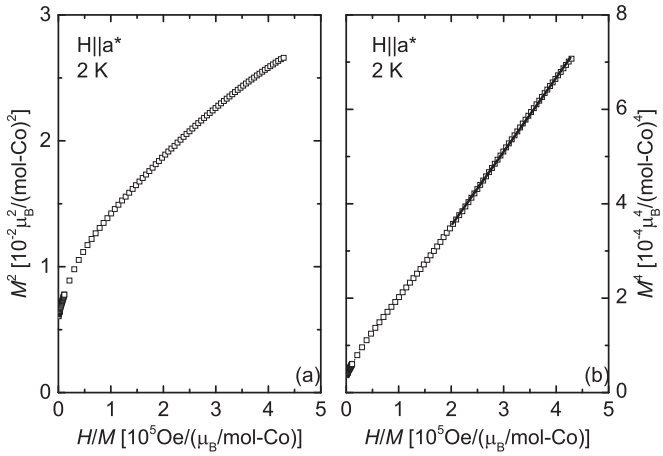

FIG. 11. (a) M^2 vs H/M plot (Arrott plot) at 2 K of $La_5Co_2Ge_3$ for magnetic field H applied along a^* direction. (b) M^4 vs H/M plot at 2 K of $La_5Co_2Ge_3$ for magnetic field H applied along a^* direction. Solid line indicates the linear fit of the data in the high-field region (28 kOe $\leqslant H \leqslant$ 70 kOe).

In this case, isotherm M^4 versus H/M is linear and the slope can be obtained. T_0 and T_A parameters can then be calculated based on Eqs. (C4b)) and (C5).

Now we apply this analysis to our measurement results. $M(H)$ curves are measured at 2 K with field H applied along different directions. In the following, we take the $M(H)$ data with $H||a^*$ (largest magnetization direction) to estimate the spin fluctuation. Figures 11(a) and 11(b) present the M^2 and M^4 as a function of H/M at 2 K for $H||a^*$, respectively. As shown in the figure, M^2 versus H/M displays a overall nonlinear behavior over the full field range (negative curvature), whereas M^4 displays linear dependence on H/M over a large field range. This suggests that, for this model, $T = 2$ K $\sim 1/2T_C$, is not in the $T \ll T_C$ limit and is rather still better fit with the T close to T_C limit. Therefore a linear fit of M^4 versus H/M data in the high-field region was performed [solid line in Fig. 11(b)] and the obtained slope is $1.56 \times 10^{-9} \frac{[\mu_B/(\text{mol Co})^5]}{\text{Oe}}$.

In the following, we estimate the ordered magnetic moment in the ground state, M_0, based on the magnetization at 2 K and the determined internal fields (B_1, B_2) behavior from μSR measurements. Magnetization at 2 K, M_{2K}, is obtained to be 0.08 μ_B/mol-Co for $H||a^*$ (see Fig. 4). Since internal field B is directly proportional to magnetization M and follows $B = B_0(1-(T/T_C)^\alpha)^\beta$, where $\alpha = 2.666$ and $\beta = 0.293$ are determined from μSR measurements, the temperature-dependent magnetization can be described as $M = M_0(1-(T/T_C)^\alpha)^\beta$. From this, M_0 is calculated to be 0.085 μ_B mol Co.

With the slope of $\frac{M^4}{H/M}$ and M_0, the fluctuation parameters are calculated to be $T_0 = 2227$ K and $T_A = 1257$ K based on Eqs. (C4b) and (C5). The ratio T_C/T_0 characterizes the degree of itinerancy. $La_5Co_2Ge_3$ gives a T_C/T_0 value of 0.0017, indicates strong itinerant nature of the magnetism. In the end, we point out that to better investigate the magnetism of $La_5Co_2Ge_3$ in the spin-fluctuation theory, further detailed measurements of $M(H)$ isotherms over a wider range of temperatures and orientations would be needed to refine our values of T_0 and T_A to further explore this model [24,25].

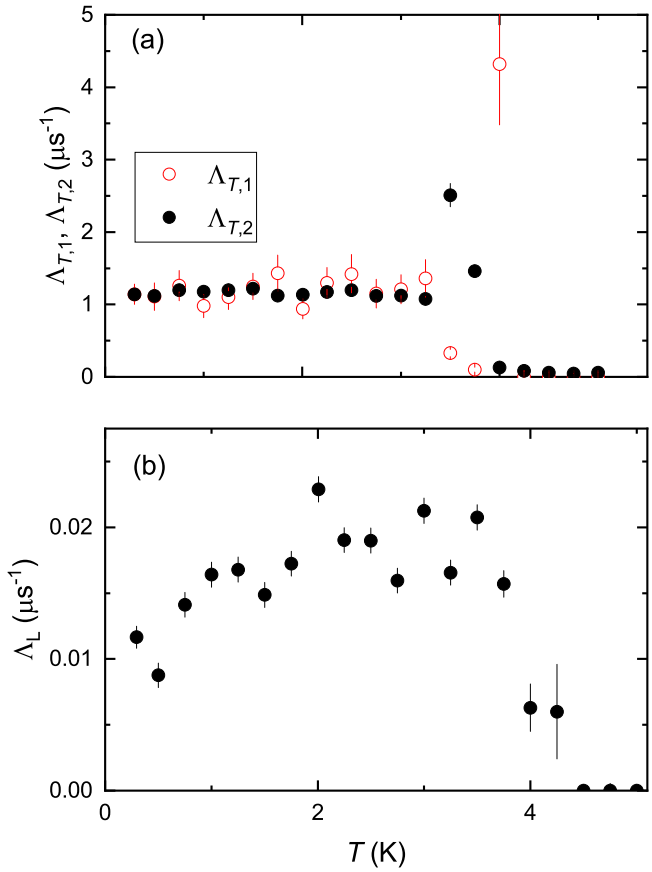

FIG. 12. (a) Temperature evolutions of the transversal relaxation rates $\lambda_{T,1}$ and $\lambda_{T,2}$. (b) Temperature evolution of the longitudinal relaxation rate λ_L.

APPENDIX D: ZF μSR DATA ANALYSIS PROCEDURE

The time evolution of the muon spin polarization $P(t)$ due to interaction with sample was described by assuming the presence two internal fields $B_{\text{int},1}$ and $B_{\text{int},2}$ with the corresponding weight f and $(1-f)$, respectively. In the case of $La_5Co_2Ge_3$, the presence of two internal fields most probably corresponds to the two muon-stopping sites. Given the rather large and complex unit cell of $La_5Co_2Ge_3$ (Fig. 9) this is not all surprising and the presence of multiple muon sites is often observed (see, e.g., Refs. [27–29] and references therein). The following functional form was used:

$$P(t) = \tfrac{1}{3}\, e^{-\lambda_L t} + \tfrac{2}{3}[f\, e^{-\lambda_{T,1} t} \cos(\gamma_\mu B_{\text{int},1} t) + (1-f)\, e^{-\lambda_{T,2} t} \cos(\gamma_\mu B_{\text{int},2}\, t)]. \quad \text{(D1)}$$

Here, $\gamma_\mu = 2\pi$ 135.5 MHz/T is the muon gyromagnetic ratio, and λ_T and λ_L are the transverse and the longitudinal exponential relaxation rates, respectively. The occurrence of 2/3 oscillating and 1/3 nonoscillating μSR signal fractions originates from the spatial averaging in powder samples, where 2/3 of the magnetic field components are perpendicular to the muon spin and cause a precession, while the 1/3 longitudinal field components do not. Note that Eq. (D1) only describes the contribution from the sample. The background contribution, which is not included in the equation, corresponds to muons stopped outside of the sample (sample

holder, cryostat walls, cryostat windows, glue, etc.). During the fit, the background contribution was described by a simple exponential relaxation function as $e^{-\lambda_{BG}t}$, where λ_{BG} is a temperature independent relaxation rate $\sim$ms^{-1}. The substantial background is the feature of all low-temperature cryostats, which depends not only on the cryostat, but also on the sample size and the amount of glue used. A fully magnetic sample in this case suggests approximately 65% sample and 35% background contributions, respectively. These numbers are quite reasonable for the amount of the sample used in our studies.

The weight of the high-field component (f) is field independent and was found to be $f \simeq 0.19$. Temperature evolutions of the transversal ($\lambda_{T,1}$ and $\lambda_{T,2}$) and longitudinal relaxation (λ_L) are presented in Fig. 12. The similar temperature dependencies of $B_{\text{int},1}$ and $B_{\text{int},2}$ (see Fig. 7 in the main text) as well as $\lambda_{T,1}$ and $\lambda_{T,2}$ (see Fig. 12) confirms the presence of two muon-stopping sites in $La_5Co_2Ge_3$.

[1] A. Szytula and J. Leciejewicz, *Handbook of Crystal Structures and Magnetic Properties of Rare Earth Intermetallics* (CRC, Boca Raton, Florida, 1994).

[2] B. T. Matthias, A. M. Clogston, H. J. Williams, E. Corenzwit, and R. C. Sherwood, Phys. Rev. Lett. **7**, 7 (1961).

[3] B. T. Matthias and R. M. Bozorth, Phys. Rev. **109**, 604 (1958).

[4] K. Kadowaki, K. Okuda, and M. Date, J. Phys. Soc. Jpn. **51**, 2433 (1982).

[5] M. Avila, S. Bud'ko, and P. Canfield, J. Magn. Magn. Mater. **270**, 51 (2004).

[6] T. Fujiwara, N. Aso, H. Yamamoto, M. Hedo, Y. Saiga, M. Nishi, Y. Uwatoko, and K. Hirota, J. Phys. Soc. Jpn. **76**, 60 (2007).

[7] E. Svanidze, J. K. Wang, T. Besara, L. Liu, Q. Huang, T. Siegrist, B. Frandsen, J. W. Lynn, A. H. Nevidomskyy, M. B. Gamża *et al.*, Nat. Commun. **6**, 7701 (2015).

[8] P. Rhodes and E. Wohlfarth, Proc. R. Soc. London A **273**, 247 (1963).

[9] P. C. Canfield and I. R. Fisher, J. Cryst. Growth **225**, 155 (2001).

[10] P. C. Canfield, Rep. Prog. Phys. **83**, 016501 (2020).

[11] Q. Lin, K. Aguirre, S. M. Saunders, T. A. Hackett, Y. Liu, V. Taufour, D. Paudyal, S. Bud'ko, P. C. Canfield, and G. J. Miller, Chem. - Eur. J. **23**, 10516 (2017).

[12] O. J. Schumann, Cologne Laue Interference Program (CLIP) (2009), http://clip4.sourceforge.net/manual.pdf.

[13] L. de Jongh and A. Miedema, Adv. Phys. **23**, 1 (1974).

[14] J. M. Santiago, C.-L. Huang, and E. Morosan, J. Phys.: Condens. Matter **29**, 373002 (2017).

[15] S. Jia, S. L. Bud'ko, G. D. Samolyuk, and P. C. Canfield, Nat. Phys. **3**, 334 (2007).

[16] V. Taufour, U. S. Kaluarachchi, R. Khasanov, M. C. Nguyen, Z. Guguchia, P. K. Biswas, P. Bonfà, R. D. Renzi, X. Lin, S. K. Kim *et al.*, Phys. Rev. Lett. **117**, 037207 (2016).

[17] U. S. Kaluarachchi, L. Xiang, J. Ying, T. Kong, V. Struzhkin, A. Gavriliuk, S. L. Bud'ko, and P. C. Canfield, Phys. Rev. B **98**, 174405 (2018).

[18] U. S. Kaluarachchi, V. Taufour, S. L. Bud'ko, and P. C. Canfield, Phys. Rev. B **97**, 045139 (2018).

[19] M. Brando, D. Belitz, F. Grosche, and T. Kirkpatrick, Rev. Mod. Phys. **88**, 025006 (2016).

[20] SMART for Windows NT/2000. Version 6.148, Bruker AXS Inc., Madison WI, USA (2013).

[21] SAINT plus. Version 8.30, Bruker AXS Inc., Madison WI, USA (2002).

[22] SHELXTL, 6.10 ed., Bruker Analytical X-ray Systems, Inc., Madison, WI (2000).

[23] L. Pauling, *The Nature of the Chemical Bond*, 3rd ed. (Cornell University Press, Ithaca, NY, 1960), p. 644.

[24] T. Moriya and Y. Takahashi, J. Phys. Soc. Jpn. **45**, 397 (1978).

[25] Y. Takahashi, *Spin Fluctuation Theory of Itinerant Electron Magnetism* (Springer, Berlin, Heidelberg, 2013).

[26] A. Arrott, PR **108**, 1394 (1957)

[27] A. Amato, P. Dalmas de Réotier, D. Andreica, A. Yaouanc, A. Suter, G. Lapertot, I. M. Pop, E. Morenzoni, P. Bonfà, F. Bernardini, and R. De Renzi, Phys. Rev. B **89**, 184425 (2014).

[28] R. Khasanov, A. Amato, P. Bonfà, Z. Guguchia, H. Luetkens, E. Morenzoni, R. De Renzi, and N. D. Zhigadlo, Phys. Rev. B **93**, 180509(R) (2016).

[29] R. Khasanov, A. Amato, P. Bonfà, Z. Guguchia, H. Luetkens, E. Morenzoni, R. De Renzi, and N. D. Zhigadlo, J. Phys.: Condens. Matter **29**, 164003 (2017).